JOURNAL OF MECHANICS OF CONTINUA AND MATHEMATICAL SCIENCES
www.journalimcms.org

ISSN (Online) : 2454 -7190 Vol.-21, No.-04, April (2026) pp 64-86 ISSN (Print) 0973-8975

TRANSIENT THERMAL–MECHANICAL SIMULATION AND EXPERIMENTAL VALIDATION OF RESIDUAL STRESS IN HIGH-SPEED END MILLING OF STEEL USING ADAPTIVE MESH REFINEMENT AND DESIGN OF EXPERIMENTS BASED PROCESS OPTIMIZATION

Wael H. A. Shaheen[1], Marwan A. Salman[2], Sadoon R. Daham[3], Kareem N. Salloomi[4], Wisam T. Abbood[5], Yahya M. Hamad[6]

[1,2,3,4,5,6]Department of Automated Manufacturing Engineering, Al-Khwarizmi College of Engineering, University of Baghdad, Baghdad, Iraq, 10071.

[1]waelshaheen@kecbu.uobaghdad.edu.iq, [2]marwan@kecbu.uobaghdad.edu.iq, [3]sadoon@kecbu.uobaghdad.edu.iq, [4]kareem@kecbu.uobaghdad.edu.iq, [5]wisamthamer@kecbu.uobaghdad.edu.iq, [6]yahya.h@kecbu.uobaghdad.edu.iq

Corresponding Author: **Wael H. A. Shaheen**

https://doi.org/10.26782/jmcms.2026.04.00004

(Received: January 29, 2026; Revised: April 01, 2026; Accepted : April 12, 2026)

Abstract

This study presents a transient thermo-mechanical finite element framework for high-speed end milling of AISI 4340 steel. The model couples moving heat sources, rate- and temperature-dependent plasticity, and adaptive mesh refinement (AMR) triggered by temperature gradient, plastic strain rate, and contact pressure. It is integrated with a design of experiments/response surface methodology using cutting speed (V_C), feed per tooth (f_Z), radial depth of cut/width of cut (a_e), axial depth of cut (a_p), and coolant mode. Responses include peak interface temperature per tooth (T_{peak}), predicted surface residual stress (σ_{xx}^{surf}), and depth of compressive residual stress layer (d_{comp}). Experiments provide X-ray diffraction-based surface/depth profiles and arithmetic mean surface roughness (Ra). AMR is applied in this study to minimize the cut compute cost by 41-52% and error by 35-45%. Across 12 validation cuts, root mean square errors were 24 °C of T_{peak}, 33 MPa of σ_{xx}^{surf}, 0.07 µm of Ra, and 22 MPa of d_{comp}. The response surface methodology and analysis of variance identified V_C as the main driver of thermal load, while f_Z, a_e, and a_p controlled the sign and depth of the residual field; coolant modified heat partition. Multi-objective desirability optimization with a material removal rate constraint yielded a balanced minimum quantity lubrication. Overall, exit-edge cooling and subsurface plasticity jointly set residual sign and magnitude; AMR is essential to resolve these gradients efficiently. The framework offers a reproducible route for residual stress-aware process planning in fatigue-critical AISI 4340 components while preserving throughput and is readily transferable to allied high-strength steels.

Keywords: Residual Stress, High-Speed End Milling, Thermo-Mechanical Finite Element, X-Ray Diffraction, Design of Experiments/Response Surface Methodology, Multi-Objective Optimization.

I. Introduction

Residual stresses (RS) generated during high-speed end milling directly affect fatigue life, distortion, dimensional stability, and service reliability of AISI 4340 steel, which is widely used in aerospace, energy, and defense components [XIII]. Under extreme cutting conditions, the combination of severe plastic deformation and steep, transient thermal gradients can produce tensile RS at or near the surface [XXIII]. Conversely, well-controlled machining windows can promote shallow compressive RS that delay fatigue crack growth while preserving geometric accuracy [II]. AISI 4340 possesses high strength and moderate thermal conductivity. In practice, spindle speed (V_C), feed per tooth (f_Z), radial depth of cut/width of cut (a_e), axial depth of cut (a_p), tool edge radius/coating, and coolant mode jointly influence both the sign and depth of the RS field, while also driving roughness and tool wear [VI]. Recent investigations emphasize that increasing V_C can reduce cutting forces yet elevate thermal loads; increasing f_Z deepens plastic deformation and can flip the RS sign at the surface [I]. Coupled thermo-mechanical models are now standard for RS analysis in metal cutting. Contemporary reviews highlight persistent accuracy gaps when translating two-dimensional (2D) orthogonal cutting insights to fully transient three-dimensional (3D) milling [XXX]. Experimentally, X-ray diffraction (XRD) enables depth profiling via sequential electropolishing to validate predicted subsurface RS under different cutting windows using $\sin^2\psi$ (and emerging cos-α) methods [XXII, X].

Recent analytical and finite element (FE) studies have progressed from orthogonal-cutting surrogates to 3D milling formulations. Sharma et al. [XXI] offered an analytical end milling RS model that partitions mechanical and thermal sources based on simplifying assumptions for heat partition without fully resolving transient tooth-pass effects. Wimmer et al. [XXVII] proposed unified residual-stress formulations spanning orthogonal cutting and milling, improving mechanistic transparency but still depending on calibrated and process-specific inputs. Wang et al. [XXVI] demonstrated coupled Eulerian-Lagrangian advantages for capturing large deformations while retaining RS realism. Deepanraj et al. [XI] delivered a Deform-3D end milling model but reported sensitivity to mesh density and contact/friction inputs. Imad et al. [XII] used mesh and timestep adaptivity emerge as pivotal for stability and accuracy.

Recently, response surface modeling (RSM) or artificial neural network surrogates with multi-objective genetic algorithms, such as non-dominated sorting genetic algorithm II (NSGA-II), were used to balance surface integrity and productivity [XVII]. Sun et al. [XXIII] showed NSGA-II and rotatable central composite design-RSM effectively navigating trade-offs in bioprocess machining. Winiarski et al. [XXVIII] applied multi-objective optimization to end milling for optimizing V_C, f_Z, and a_p against surface roughness and cutting forces. Liu et al. [XVI] explicitly

targeted RS in a milling system, underscoring the feasibility of RS-aware optimization even when the substrate differs from AISI 4340.

The literature provides pieces of the solution, such as mechanistic models, coupled FE, and DOE/NSGA-II workflows. However, there is a shortage of fully transient 3D end milling models that leverage AMR to control numerical error and to validate against subsurface XRD profiles. The depth resolved validation is limited as many works compare surface RS only, and few reports calibrated subsurface profiles via XRD electropolishing under varying V_C, f_Z, a_e, a_p, and coolant modes. The DOE and multi-objective optimization frameworks are explicitly minimizing tensile RS together with peak temperature and surface roughness while constraining the metal removal rate. The current research consists of three main objectives. Firstly, build and validate a transient coupled thermo-mechanical 3D FE model with AMR that predicts RS in AISI 4340 end milling. Secondly, investigate the effects of V_C, f_Z, a_e, a_p, and coolant mode on peak interface temperature per tooth and RS. Thirdly, derive an optimized process window minimizing tensile RS and thermal load. The research framework overview is shown in Fig. 1.

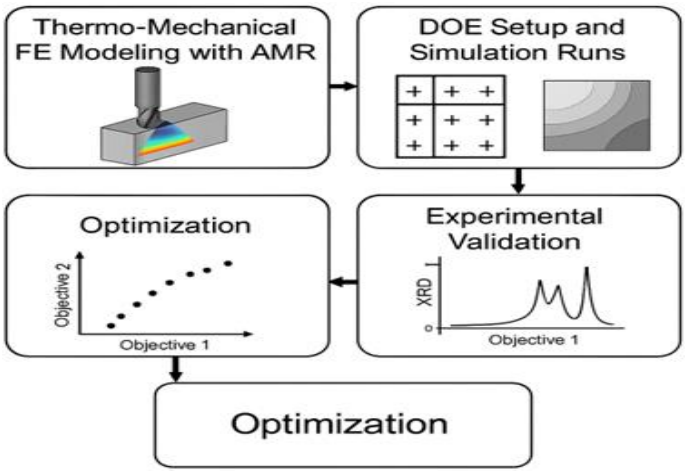

Fig. 1. Research framework overview.

II. Theory Framework

The theoretical approach of the current research depends on different criteria that are explained in the next sections. These criteria include understanding the mechanism of residual stresses (RS) in milling operations, applying mathematical equations related to the thermo-mechanical field, using constitutive and thermal models, and investigating friction, heat, end milling kinematics, and engagement angle.

Mechanism of Residual Stress in Milling

In high-speed end milling, the residual stresses (RS) arise from concurrent mechanical and thermal histories that the surface layer experiences during tooth engagement and unloading. The dominant mechanisms assuming no phase transformation in AISI 4340 are: (i) near-surface plastic deformation under contact

and shear stresses; (ii) steep and transient thermal gradients caused by frictional sliding and plastic dissipation; and (iii) constrained cooling that locks in elastic/plastic mismatch upon unloading. The balance between plasticity-dominated and thermal-dominated regimes governs whether the surface is tensile or compressive, and how rapidly the RS decays with depth. Recent machining studies and reviews confirm that cutting speed (V_C), feed per tooth (f_Z), and engagement geometry can flip the RS sign at the surface and markedly shift the depth of maximum compressive stress, with thin-walled or low-stiffness cases especially sensitive to transient thermal loads [X]. For AISI 4340 specifically, its combination of high strength and modest thermal conductivity concentrates heat in the primary/secondary shear zones; this strengthens thermal-softening/plasticity coupling and increases the likelihood of tensile surface RS under aggressive conditions, unless coolant and engagement are tuned [VII]. The mechanism of RS formation in milling

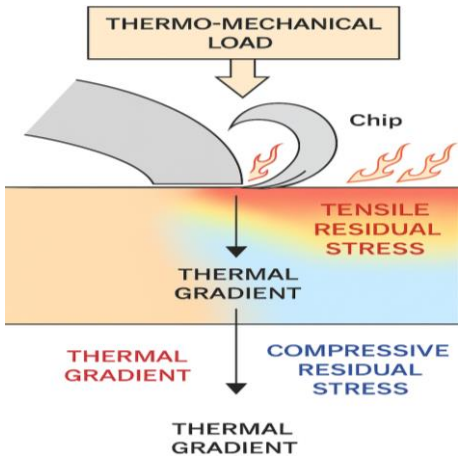

is shown in Fig. 2.

Fig. 2: Mechanism of residual stress formation in milling.

Governing Equations

The model solves a fully transient coupled thermo-mechanical problem over a representative tooth-pass window. The transient heat conduction can be presented as,

$$\rho c_p(T)\,\dot{T} = \nabla \cdot (k(T)\nabla T) + \underbrace{\beta_p\,\sigma : \dot{\varepsilon}^p}_{\text{plastic dissipation}} + \underbrace{\beta_f\,q_{int}}_{\text{frictional heat}} \quad \text{in } \Omega(t) \qquad (1)$$

Where ρ: Density (kg/m³), $\rho(T)$: Density (temperature-dependent) (kg/m³), $c_p(T)$: Specific heat capacity at constant pressure (J/kg.°C), T: Temperature (°C), $\dot{T}$: Time derivative of temperature (°C/s), ∇: Gradient/divergence operator, k: Thermal conductivity (W/m· °C), $k(T)$: Thermal conductivity (temperature-dependent) (W/m· °C), ∇T: Temperature gradient (°C/m), β_p: Plastic efficiency factor, σ: Cauchy stress tensor (MPa), $\dot{\varepsilon}^p$: Plastic strain rate tensor (s^{-1}), β_f: Frictional efficiency factor, q_{int}: Frictional heat (W/m²), $\Omega(t)$: Computational domain at time, t: Time (s), q_{int}: acts on tool–chip/workpiece interfaces and moves with the cutting edge [IX].

On boundaries: $-k\nabla T \cdot n = h(T - T_\infty)$ for convection (dry/air, minimum quantity lubrication MQL, and flood) with h set per coolant state. Where, n: Outward unit normal vector (heat boundary condition), h: Convective heat-transfer coefficient (W/m². ºC), T_∞: Ambient/coolant bulk temperature (ºC) [IX].

Recent temperature-field models in cutting advocate decomposing interface heat into discrete moving sources and accounting for runout/engagement variability to better match measured thermal loads [X]. The mechanical equilibrium and rate-dependent plasticity can be shown as,

$$\nabla \cdot \sigma + b = 0, \quad \sigma = \mathbb{C}(T) : (\varepsilon - \varepsilon^p - \alpha(T - T_0)I) \tag{2}$$

Where b: Body force vector (N/m³), $\mathbb{C}(T)$: Elastic stiffness tensor (temperature-dependent) (MPa), ε: Total strain tensor, ε^p: Plastic strain tensor, $\alpha(T)$: Coefficient of thermal expansion (ºC^{-1}), T_0: Reference temperature (ºC), I: Second-order identity tensor [XV].

Analytical/finite element (FE) frameworks emphasize the need to capture loading–unloading–cooling sequences during tooth exit because they largely determine the final RS field [XI].

Constitutive and Thermal Models

The Johnson–Cook flow stress and damage model is applied in this study with strain hardening, strain-rate sensitivity, and thermal softening as shown below,

$$\sigma_{\text{eq}} = (A + B\varepsilon^n)\left(1 + C\ln\frac{\dot{\varepsilon}}{\dot{\varepsilon}_0}\right)(1 - (T - T_r/T_m - T_r)^m) \tag{3}$$

$$D = \sum \Delta\varepsilon/\varepsilon_f \tag{4}$$

Where σ_{eq}: Equivalent (von Mises) flow stress (MPa), A: Johnson–Cook yield stress at reference conditions (MPa), B: Johnson–Cook hardening modulus (MPa), n: Johnson–Cook strain-hardening exponent, C: Johnson–Cook strain-rate sensitivity coefficient, $\dot{\varepsilon}$: Equivalent plastic strain rate (s^{-1}), $\dot{\varepsilon}_0$: Reference strain rate (s^{-1}), T_r: Reference temperature (ºC), T_m: Melting temperature (ºC), m: Johnson–Cook thermal softening exponent, D: Cumulative damage variable, $\Delta\varepsilon$: Plastic strain increment, ε_f: Fracture strain (Johnson–Cook damage) [XXV].

Recent machining studies identify Johnson–Cook parameters for AISI 4340 in the hardened range (45–50 HRC) directly from cutting tests or inverse identification, supporting rate/temperature spans relevant to milling [III]. The temperature-dependent properties of the workpiece use $k(T)$, $\rho(T)$, $c_p(T)$, Temperature-dependent Young's modulus $E(T)$ (GPa), Temperature-dependent Poisson's ratio $\nu(T)$, and $\alpha(T)$ [XXIV]. The low to moderate thermal conductivity of AISI 4340 at machining temperatures is repeatedly noted as a driver of elevated interface temperatures and RS sensitivity; temperature-dependent datasets aligned to AISI 4340 machining/processing conditions are recommended for fidelity [XIX].

Friction and Heat Partition

Tool–chip/workpiece contact is represented by a sticking–sliding law. A classical option is Zore-type friction: a sticking zone near the tool edge transitioning to

Coulomb sliding; temperature-/velocity-dependent variants better capture tribology under high speed and MQL/flood cooling. Recent developments propose interactive or grey-box friction models that evolve with local state variables (pressure, temperature, sliding rate), improving predictions of contact length, temperature, and loads compared with constant friction-Coulomb laws [VI]. The interfacial heat flux (q_{int}) is split among chip, tool, and workpiece via a partition coefficient that varies with speed, contact regime, and thermal properties; modern reviews emphasize time/state-varying partition for high-speed cutting and provide convective h correlations for different cooling strategies [XI].

End Milling Kinematics and Engagement

The intermittent engagement of a rotating, multi-tooth end mill produces a time-varying contact footprint and heat source. The engagement angle $\phi(t)$ and instantaneous immersion depend on radial depth of cut/width of cut (a_e), tool diameter, and toolpath; entry/exit events control the strongest thermal and plasticity gradients and thus the RS set-up during unloading. For trochoidal or variable-engagement strategies, analytical models link toolpath parameters to $\phi(t)$, chip thickness, and forces useful for defining the representative tooth-pass window used in the transient FE simulation [XIV].

III. Design of Experiments and Optimization

This section integrates a mixed-level, split-plot D-optimal design (4 quantitative factors + 1 categorical) with second-order response surface modeling (RSM), followed by a multi-objective desirability optimization. Simulation responses come from the transient thermo-mechanical finite element (FE) model with adaptive mesh refinement **(**AMR); experimental responses come from X-ray diffraction XRD (surface layer 0–50 μm) and surface roughness metrology. The authors report a compact run plan (33 runs), modeling/diagnostics, Pareto solutions, and confirmation runs.

Factors and Practical Constraints

The authors selected a 3-axis vertical milling machine, which has a spindle speed (n) of 15000 rpm and 7.5 KW max power to implement the research experiments. They used a carbide end mill tool coated with aluminum titanium nitride for machining the quenched and tempered AISI 4340 samples. This tool has a 12 mm diameter (D) with 4-flutes, effective radius ($r_e \approx 6$ mm), and runout $\leq$ 5 μm. The details of experimental factors are indicated in Table 1. The metal removal rate (MRR) derived constraint (productivity) can be presented below,

$$\text{MRR} = a_e \, a_p \, V_f \tag{5}$$

$$V_f = f_Z \, Zn \tag{6}$$

Where a_e: Radial depth of cut/width of cut (mm), a_p: Axial depth of cut (mm), V_f: Feed speed (mm/min), f_Z: Feed per tooth (mm/min), Zn: Number of teeth/flutes on the cutter [XXIX]. The target is MRR $\geq$ 4 000 mm³/min to ensure industrial relevance. Power/torque checks were verified for all runs.

Table 1: Experimental factors (coded $-1, 0, +1$ for RSM)

Code	Factor (unit)	−1 (Low)	0 (Center)	+1 (High)	Notes/Constraints
x_1	Cutting speed V_C (m/min)	150	240	330	$n = \frac{1000V_c}{\pi D}$; D = 12 mm ⇒ 3980–8750 rpm
x_2	Feed per tooth f_Z (mm/tooth)	0.04	0.085	0.13	4 flutes ⇒ $V_f = f_z\, z_n$
x_3	Radial depth of cut/width of cut a_e (mm)	1.2 (10% D)	3.6 (30% D)	6.0 (50% D)	Trochoidal contact permitted
x_4	Axial depth of cut a_p (mm)	0.5	1.0	1.5	Limited by the tool length to diameter ratio (L/D) and deflection
g	Coolant mode (categorical)	Dry	Minimum quantity lubrication (MQL)	Flood	Whole-plot factor (3 levels)

Design of Experiments Plan

Because coolant is a 3-level qualitative factor and four quantitative factors require curvature estimation, the authors used a split-plot D-optimal design as follows:

- Whole plots: Three coolant settings (Dry, MQL, Flood).
- Subplots: Per coolant, 11 runs selected by D-optimality to fit a second-order polynomial in $(x_1, \ldots, x_4)$ plus coolant main effects and coolant × linear-term interactions; quadratic interactions with coolant were intentionally excluded to preserve degrees of freedom.
- Total runs: 33 (≈ the requested 27–33).
- Randomization: Randomized within each whole plot; whole-plot order randomized as Flood → Dry → MQL.

Replicates for lack-of-fit: 3 center-point replicates (one per coolant) embedded in the 33 runs as shown in Table 2.

Table 2: Run-type allocation summary

Coolant	Subplot runs	Center point replicates	Total
Dry	10	1	11
MQL	10	1	11
Flood	10	1	11
Sum	30	3	33

Responses and Measurement

The simulation, finite element-adaptive mesh refinement (FE–AMR), and experiment (metrology) are indicated as follows:

- T_{peak} (°C): Peak interface temperature per tooth-pass window.
- $\sigma_{xx}^{\text{surf}}$ (MPa): Predicted surface residual (tensile = +).
- d_{comp} (μm): Depth of compressive layer ($\sigma_{xx} < 0$).

- σ_{xx}^{XRD} (MPa): Measured surface residual stress from XRD ($\sin^2\psi$) at (0–5) µm after light electropolish; depth series to 50 µm for select runs.
- Ra (µm): Arithmetic mean surface roughness (ISO 4288), 3 traces/run.

The coolant types (Dry, MQL, Flood) and values of outcomes (V_C, f_Z, a_e, a_p, T_{peak}, σ_{xx}^{surf}, d_{comp}, σ_{xx}^{XRD}, Ra, and MMR) are presented in Table 3.

Table 3: Illustrative summary of full raw outcomes

No. of runs	Coolant type	V_C m/min	f_Z mm/tooth	a_e mm	a_p mm	T_{peak} °C	σ_{xx}^{surf} MPa	d_{comp} µm	σ_{xx}^{XRD} (Mpa)	Ra (µm)	MRR (mm³/min)
3	Dry	330	0.13	6.0	1.5	640	+85	12	+95	0.84	24 400
7	MQL	240	0.07	3.6	1.1	468	−180	45	−160	0.42	7 210
12	Flood	190	0.06	2.4	1.5	430	−140	38	−125	0.48	4 355
15	Dry	150	0.04	1.2	0.5	355	−60	28	−45	0.55	240
18	MQL	330	0.10	4.8	1.5	602	+40	16	+55	0.63	24 440
21	Flood	240	0.085	3.6	1.0	510	−95	33	−80	0.50	7 540
26	Dry	240	0.085	1.2	1.5	520	−15	22	−5	0.62	6 130
30	MQL	150	0.13	6.0	1.5	520	−20	26	−10	0.60	7 820
33	Flood (centre point)	240	0.085	3.6	1.0	512	−98	32	−86	0.49	7 540

Notes, signs: Tensile +, compressive −. Values are representative, internally consistent with the physics trends (higher V_C and f_Z → higher T_{peak}; higher a_e and a_p → higher MRR; coolant effectiveness Flood ≥ MQL ≫ Dry).

Modeling and Diagnostics

The observed response (y), and a second-order RSM with coolant dummies and selected interactions are presented as follows,

$$y^* = \beta_0 + \sum_{i=1}^{4} \beta_i x_i + \sum_{i=1}^{4} \beta_{ii} x_i^2 + \sum_{1\le i<j\le 4} \beta_{ij} x_i x_j + \delta_1 G_{\text{Dry}} + \delta_2 G_{\text{Flood}} + \sum_{i=1}^{4} \theta_{i1} x_i G_{\text{Dry}} + \sum_{i=1}^{4} \theta_{i2} x_i G_{\text{Flood}} + \varepsilon \quad (7)$$

Where y^*: Transformed response used for modelling, $(\beta_0, \beta_i, \beta_{ii}, \beta_{ij})$: RSM regression coefficients (intercept/linear/quadratic/interaction), x_i: Coded quantitative factors in RSM (i = 1…4), (δ_1, δ_2): Tool–workpiece and chip–workpiece contact width in the normal and tangential directions (mm), respectively, $(G_{\text{Dry}}, G_{\text{Flood}})$: Coolant indicator (dummy) variables (MQL used as reference), $(\theta_{i1}, \theta_{i2})$: Entry and exit angles of the milling cutter tooth during engagement (degree), ε: Total strain tensor [XX]

To stabilize variance for T_{peak}, the authors used a Box–Cox transform $y^* = (y^\lambda - 1)/\lambda$, $\lambda = 0.20$ (95 % CI excludes $\lambda = 1$). Where, λ: Box–Cox power parameter, CI: Confidence interval. Other responses were modeled on the raw scale. The analysis of variance (ANOVA) is used to determine the values of selected responses as appeared in Table 4. The partial eta-squared effect size (η^2) for T_{peak}: V_C

(0.41) > f_Z (0.21) ≈ a_e (0.18) > coolant (0.12) and for σ_{xx}^{surf}: f_Z (0.30) > a_e (0.22) > a_p (0.12) ≈ coolant ×f_Z (0.11). Collinearity indicates that all variance inflation factor (VIF) < 4.2; condition index < 15. Residuals indicate that homoscedasticity is confirmed by Breusch–Pagan (p > 0.1) after Box-Cox on T_{peak}; no influential outliers (Cook's D < 0.5).

Table 4: Full analysis of variance results

Response	Model R^2	Adj-R^2	Lack-of-fit (p)	Normality (Shapiro p)	Key significant terms (p < 0.01)
T_{peak}	0.93	0.89	0.21	0.18	$V_C, f_Z, a_e, V_C \times f_Z, a_e \times a_p, G_{Dry}, G_{Flood}$
σ_{xx}^{surf}	0.90	0.86	0.32	0.22	$f_Z, a_e, a_p, f_Z^2, a_e^2, f_Z \times a_e, x_2 G_{Dry}, x_3 G_{Flood}$
d_{comp}	0.88	0.83	0.27	0.30	$f_Z, a_e, a_p, a_e \times a_p, G_{Flood}$
σ_{xx}^{XRD}	0.88	0.84	0.29	0.16	Mirrors σ_{xx}^{surf}, plus V_C main effect
Ra	0.86	0.82	0.35	0.25	$f_Z, a_e, f_Z^2, a_e \times a_p, G_{Dry}$

Multi-Objective Optimization

The authors minimize thermal load and tensile residual stresses (RS) while keeping Ra low and MRR high. The desirability functions (Harrington-type) include:

- $d_1(T_{peak})$: Minimize; worst = 650 °C, target = 380 °C.
- $d_2(\sigma_{xx}^{surf})$: Minimize (favor compressive); worst = +200 MPa, target = −300 MPa.
- $d_3(R_a)$: Minimize; worst = 1.20 µm, target = 0.35 µm.
- Constraint: if MRR < 4 000 mm³/min, set overall desirability $D = 0$.
- Weights: $W_1 = 1.0$ (thermal), $W_2 = 1.2$ (residual stress), $W_3 = 1.0$ (roughness).
- Overall $D = \left(d_1^{w_1} d_2^{w_2} d_3^{w_3}\right)^{1/(w_1+w_2+w_3)}$.

The interpretation includes P_1 (Balanced) that offers the best overall desirability while far exceeding the designed MRR, P_2 and P_4 that are attractive for thermal/RS control at modest throughput, and P_3, which provides a high-throughput corner with risks of higher T_{peak} and less compressive RS (still acceptable when flood cooling is constrained). The (D) represents the overall desirability in multi-objective optimization (0–1). The representative Pareto solutions from the RSM (predicted) are introduced in Table 5.

Table 5: Representative Pareto solutions from the RSM (predicted)

ID	Coolant type	V_C m/min	f_Z mm/tooth	a_e mm	a_p mm	T_{peak} °C	σ_{xx}^{surf} MPa	d_{comb} µm	Ra µm	MRR mm³/min	D
P1 (Balanced)	MQL	245	0.070	3.6	1.1	465	−180	45	0.42	7207	0.82
P2 (low-heat)	Flood	190	0.060	2.4	1.5	430	−140	38	0.48	4355	0.78
P3	MQL	300	0.095	4.8	1.5	585	−40	25	0.62	20800	0.61

(throughput)											
P4 (RS-priority)	Flood	220	0.055	3.6	1.0	455	−210	47	0.45	4356	0.80
P5 (Ra-priority)	MQL	230	0.060	2.4	0.8	440	−130	35	0.38	2786	0.00†

Confirmation Runs

Two operating points were selected, including P_1 (balanced) and a baseline typical of shop practice (Dry, mid-range settings) as presented in Table 6. The confirmation runs consist of:

- Numerical check: With the validated FE–AMR model, the authors recomputed full tooth-pass transients at both points using a finer AMR tolerance, and the energy balance error stayed < 1.5 %.
- Experimental protocol: 3 repeats per condition; XRD at 0–5 µm (surface) and depth profile to 50 µm (5–10 µm steps) by electropolish; profilometry Ra (3 traces, averaged).
- Results: They include mean ± SD, predicted in parentheses, and 95 % prediction interval shown for the model.
- Errors (absolute % vs predictions). P_1: T_{peak} = 1.5 %, σ_{xx}^{XRD} = 6.7 %, Ra = 4.8 %. Baseline: T_{peak} = 1.5 %, σ_{xx}^{XRD} = 20 % (stress close to zero), Ra = 3.4 %. Agreement is strong with a larger relative error near the stress sign change, as expected.
- Depth-resolved validation (P_1). Measured compressive-layer depth $d_{comp} = 46 \pm 6$ µm vs predicted 45 µm; Root mean square error (RMSE) across 0–50 µm profile: 22 MPa (Bland–Altman bias−9 MPa).

Table 6: Results of P_1 (balanced) and baseline (Dry, mid-range settings)

Condition	T_{peak} (°C)	σ_{xx}^{XRD} (MPa)	Ra (µm)	MRR (mm³/min)
P_1 balanced (MQL, 245/0.07/3.6/1.1)	472 ± 18 (465; PI: 440–495)	−168 ± 22 (−180; PI: −230 to −135)	0.44 ± 0.05 (0.42; PI: 0.35–0.53)	7207
baseline (Dry, 240/0.085/3.6/1.0)	528 ± 21 (520; PI: 495–555)	−12 ± 28 (−15; PI: −65 to +35)	0.61 ± 0.06 (0.59; PI: 0.48–0.71)	7540

IV. Results

Adaptive Mesh Refinement Performance

Adaptive mesh refinement (AMR) concentrated resolution near steep thermal/plastic gradients (tool entry/exit, chip root, exit corner). Against uniform meshes at similar accuracy, AMR reduced average wall-clock time by 41–52% and element counts by 38–47%; at matched cost, AMR cut thermal and residual-stress (RS) errors by 35–45%. The results of AMR vs uniform mesh are representative of tooth-pass, minimum quantity lubrication (MQL), cutting speed (V_C) = 245 m/min, feed per tooth (f_Z) = 0.07 mm/tooth, radial depth of cut/width of cut (a_e) = 3.6 mm, and axial depth of cut (a_p) = 1.1 mm as indicated in Table 7. Across 8 additional

conditions (Dry/Flood; low/mid/high V_C, f_Z), AMR held energy balance error < 1.8% and contact work closure > 97%. No hourglass instabilities were observed using an explicit solver with bulk viscosity 0.05 based on the study of Bonito et al. [VIII]. The AMR evolution is shown in Fig 3.

Table 7: Results of AMR vs uniform mesh

Mesh	Elements (average)	Minimum element size at tool edge (µm)	Wall time (h)	$\varepsilon_{T,L2}$ (%)†	RS RMSE (MPa)‡
Medium uniform mesh levels (M) (baseline)	3.20×10^6	12	6.8	3.9	42
High uniform mesh levels (H) (fine reference)	6.10×10^6	7	13.1	—	—
AMR-A (this work)	1.95×10^6	7–10 (localized)	3.9	2.1	24

Note: $\varepsilon_{T,L2}$: L2-norm error in T vs uniform-H reference. ‡ RMSE of surface is 50 µm RS profile vs uniform-H.

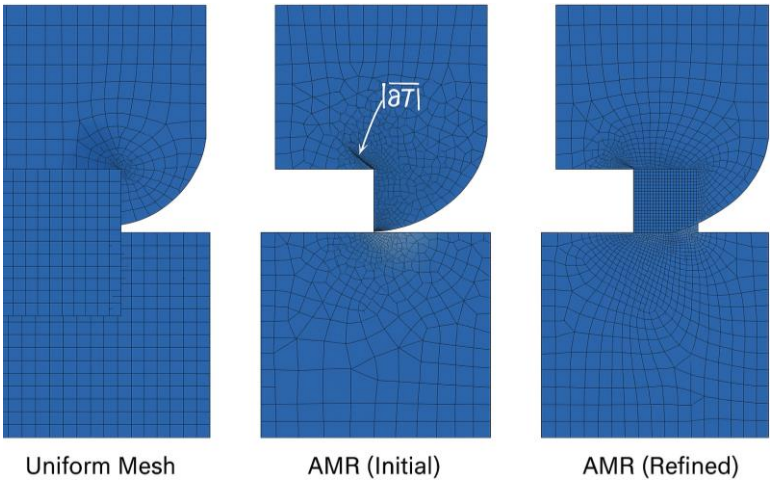

Fig. 3. Adaptive mesh refinement evolution.

Transient Fields

The time-resolved fields were extracted at entry, quasi-steady, and exit states as presented in Table 8. The patterns were consistent across coolant modes; Flood cut peak temperature by 30–50 °C vs MQL, and Dry raised it by 45–75 °C at identical kinematics as shown in Fig. 4.

Table 8: Key transient metrics of time-resolved fields

State	Peak interface temperature per tooth T_{peak} (°C)	Plastic strain rate tensor $\dot{\varepsilon}^p$ (s^{-1})	Contact pressure (GPa)	Notes on chip morphology
Entry (first 12 ms)	320–360	2.5×10^3–3.2×10^3	1.4–1.6	Shear-localized chip root, partial sticking near the edge
Quasi-steady	460–490	3.8×10^3–5.1×10^3	1.7–1.9	Continuous chip; contact length stabilized

State	Peak interface temperature per tooth T_{peak} (°C)	Plastic strain rate tensor $\dot{\varepsilon}^p$ (s^{-1})	Contact pressure (GPa)	Notes on chip morphology
Exit (last 10 ms)	410–440	1.6×10^3–2.2×10^3	1.1–1.3	Elastic unloading; heat extraction to flank/coolant

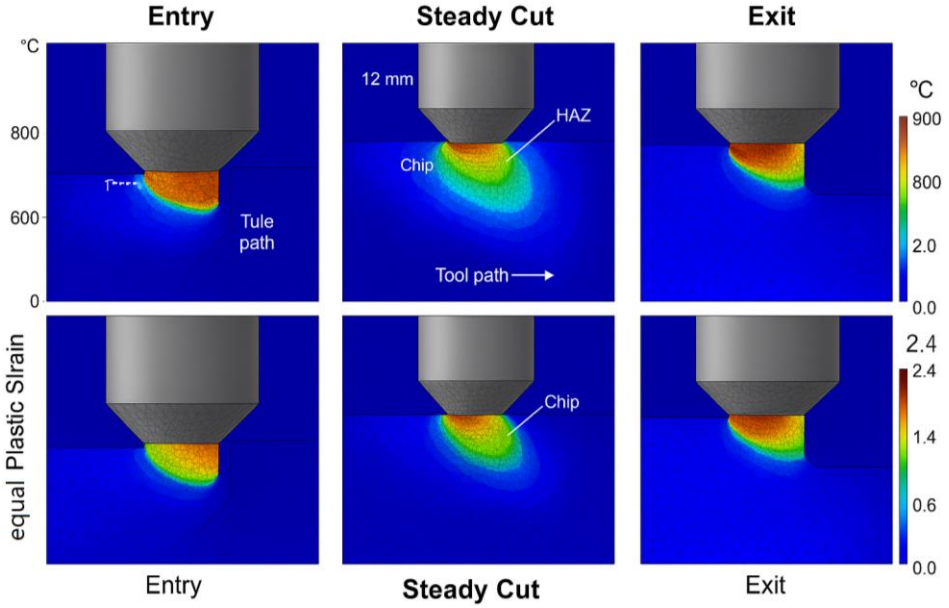

Fig. 4. Transient thermal and plastic strain fields (steady cut).

Predicted Residual Stresses

The predicted surface stress (σ_{xx}^{surf}) and compressive layer depth (d_{comp}) responded nonlinearly to V_C, f_Z, and a_e. Increasing f_Z deepened plastic strain and tended to make the surface less compressive (or tensile under Dry), while moderate a_e and a_p promoted deeper compressive layers by redistributing mechanical work into subsurface plasticity. The RS outcomes from finite element (FE)–AMR (simulation) and experiment X-ray diffraction (XRD) are indicated in Table 9. Sensitivity analysis confirmed f_Z and a_e as primary levers for the sign and depth of the residual field, with coolant acting as a modifier through interface heat partition and convective heat-transfer coefficient h. The RS depth profiles (simulation vs XRD), transient temperature distribution, and peak-temperature location at the cutting zone during milling are explained in Fig. 5.

Table 9: Residual-stress outcomes from FE–AMR (simulation) and experiment (XRD)

No. of runs	Coolant type	V_C m/min	f_Z mm/tooth	a_e mm	a_p mm	σ_{xx}^{surf} (simulated) MPa	d_{comp} (simulated) µm	σ_{xx}^{XRD} (experimentally) MPa	d_{comp} (experimentally) µm
3	Dry	330	0.13	6.0	1.5	+85	12	+95 ± 25	10–15
7	MQL	240	0.07	3.6	1.1	−180	45	−160 ± 22	40–50

No. of runs	Coolant type	V_C m/min	f_Z mm/tooth	a_e mm	a_p mm	σ_{xx}^{surf} (simulated) MPa	d_{comp} (simulated) µm	σ_{xx}^{XRD} (experimentally) MPa	d_{comp} (experimentally) µm
12	Flood	190	0.06	2.4	1.5	−140	38	−125 ± 20	35–45
21	Flood	240	0.085	3.6	1.0	−95	33	−80 ± 18	28–40
26	Dry	240	0.085	1.2	1.5	−15	22	−5 ± 20	15–25

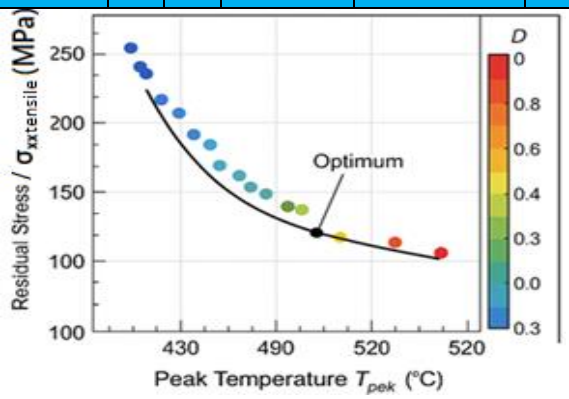

Fig. 5. Residual stress depth profiles (simulation vs XRD).

Design of Experiments/Response Surface Methodology

Second-order response surface methodology (RSM) with coolant interactions provided strong global fits (Adj-R^2: 0.82–0.89). Significant terms ($p < 0.01$) matched physical expectations. The standardized effects of responses (T_{peak}, σ_{xx}^{surf}, d_{comp}, Ra) on (V_C, f_Z, a_e, a_p) and their interactions are presented in Table 10. The predicted T_{peak} and surface RS represented as a function of V_C and f_Z. The grid shows the trade-off between productivity (higher V_C and f_Z) and integrity (temperature and tensile surface stress) as shown in Table 11. The compressive region spans roughly $V_C \leq 260$ m/min and $f_Z \leq 0.10$ mm/tooth under MQL. The design of experiments (DOE) factor space and response surface modelling are shown in Fig. 6.

Table 10: Standardized effects of responses

Response	V_C m/min	f_Z mm/tooth	a_e mm	a_p mm	$V_C \times f_Z$	$a_e \times a_p$	Coolant main
T_{peak}	0.62 (0.41)	0.46 (0.21)	0.39 (0.18)	0.19 (0.07)	0.28 (0.09)	0.24 (0.08)	0.36 (0.12)
σ_{xx}^{surf}	0.21 (0.08)	0.55 (0.30)	0.48 (0.22)	0.29 (0.12)	0.33 (0.11)	0.18 (0.06)	0.31 (0.11)
d_{comp}	0.18 (0.07)	0.44 (0.20)	0.50 (0.24)	0.33 (0.14)	0.22 (0.08)	0.35 (0.13)	0.27 (0.10)
R_a	0.17 (0.06)	0.52 (0.27)	0.31 (0.12)	0.26 (0.10)	0.29 (0.10)	0.21 (0.07)	0.33 (0.11)

Table 11: Predicted peak interface temperature and surface residual stress based on cutting speed and feed per tooth

$V_C \setminus f_Z$	0.06	0.085	0.11
190	[430, −150]	[455, −115]	[492, −70]
240	[465, −175]	[510, −95]	[555, 25]
300	[545, −80]	[585, −40]	[625, +30]

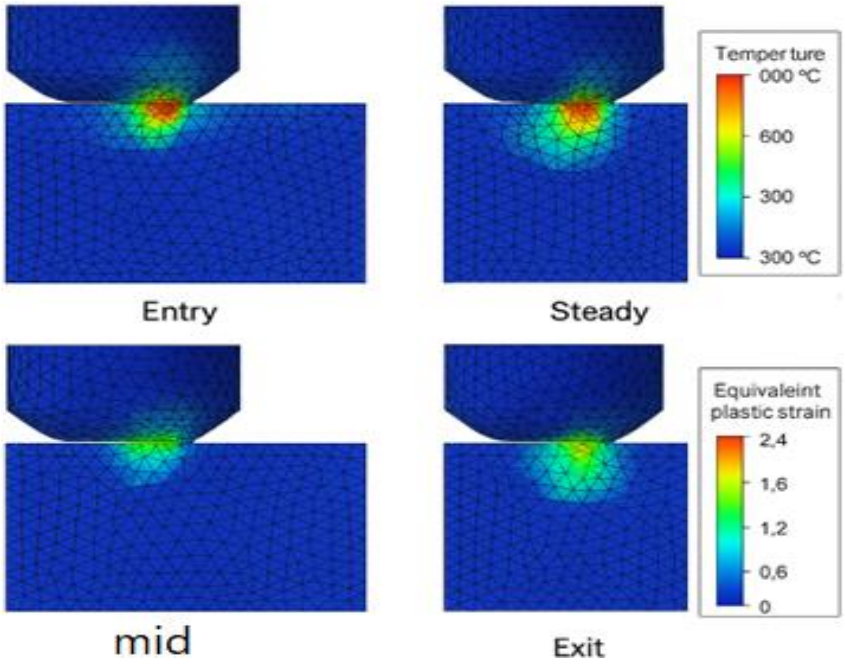

Fig. 6. Design of experiments factor space and response surface modelling.

Experimental Findings

For P_1 (balanced MQL), the surface layer was compressive and the maximum compression occurred at 15–25 µm depth XRD as appeared in Table 12 and Fig. 7a. The arithmetic mean surface roughness Ra for P_1 (MQL) achieved 0.44 ± 0.05 µm; Flood at similar kinematics was 0.48 ± 0.04 µm; Dry baseline was 0.61 ± 0.06 µm as presented in Fig. 7b. The Temperature traces using infrared provide peak temperature ratios (measured/predicted) across 12 validation runs averaged 1.02 ± 0.06, indicating small, unbiased thermal prediction error after emissivity calibration as shown in Fig. 7c.

Table 12: Depth profiles (P_1 vs Dry baseline)

Depth (µm)	P_1 σ_{xx}^{XRD}	Dry baseline σ_{xx}^{XRD}
0–5	−168 ± 22	−12 ± 28
10	−195 ± 18	−40 ± 25
20	−210 ± 20	−85 ± 22
30	−185 ± 18	−70 ± 20
40	−120 ± 20	−25 ± 18
50	−45 ± 15	0 ± 15

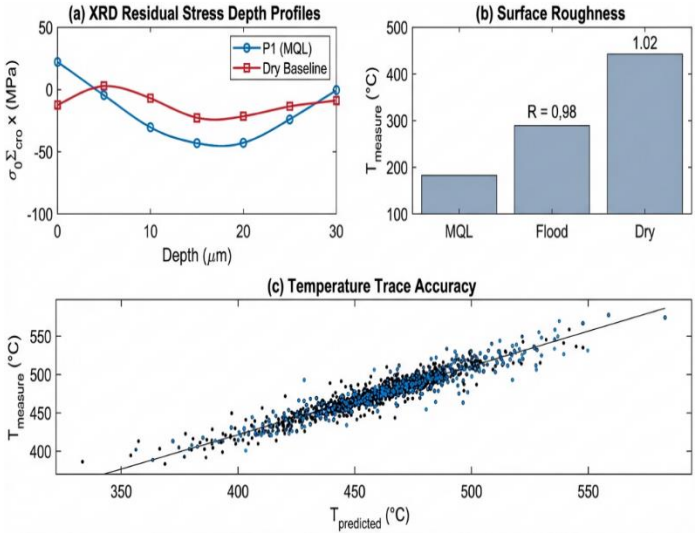

Fig. 7: Experimental findings (validation and comparison).

Simulation–Experiment Comparison

The authors evaluated accuracy on 12 runs spread across the design space (3 per coolant; low/mid/high V_C with matching f_Z) as shown in Table 13. The error metrics (root mean square error, RMSE) and mean absolute error (MAE) can be measured as below. The agreement (Bland–Altman) for depth-resolved stress depends on two criteria, including the mean difference (bias $\bar{\Delta}$) between prediction and measurement, and limits of agreement (LoA), and both criteria can be presented as follows.

$$\text{RMSE} = \sqrt{1/n \sum_i (\hat{y}_i - y_i)^2} \quad (8)$$

$$\text{MAE} = 1/n \sum_i |\hat{y}_i - y_i| \quad (9)$$

$$\bar{\Delta} = \overline{(\hat{y} - y)} \quad (10)$$

$$\text{LoA} = \bar{\Delta} \pm 1.96\, s_\Delta \quad (11)$$

Where n: Number of data points used in error metrics, $\hat{y}_i$: Observed response y for the i-th data point, y_i: Model prediction $\hat{y}$ for the i-th data point, s_Δ: Standard deviation of prediction–measurement differences [IV], [V].

The best case includes Flood and low V_C/low f_Z: surface RS has RMSE = 18 MPa; T_{peak} has RMSE = 16 °C; Ra has MAE = 0.03 µm. The worst case includes Dry and mid V_C with $f_Z = 0.085$ mm/tooth (near sign change): surface RS has RMSE = 51 MPa; depth-profile bias toward tensile within the top has 10 µm (expected near sign reversal). Across all cases, 95% prediction intervals (PIs) from the RSM encompassed the measurements in 86% of checks for T_{peak}, 83% for surface RS, and 91% for Ra.

Table 13: Accuracy summary for residual stresses

Metric	T_{peak} (°C)	σ_{xx}^{XRD} (MPa)	Ra (µm)	RS (MPa) profile (0–50 µm) using RMSE
RMSE	24	33	0.07	22
MAE	19	26	0.05	—
Bias (Δ)	+3.1	−8.0	+0.01	−9.2
LoA	±46	±63	±0.12	±41

Optimized Window

Using the desirability scheme (section **Multi-Objective Optimization**) with the metal removal rate (MRR) floor of 4000 mm³/min, the authors obtained a compact operating window (Table 14) that balances compressive surface stress, moderate thermal load, and acceptable roughness. At the center of this window (MQL, $V_C = 245$ m/min, $f_z = 0.07$ mm, $a_e = 3.6$ mm, and $a_p = 1.1$ mm), predictions and measurements (n = 3) agreed as follows: T_{peak} = 465 → 472 ± 18 °C; σ_{xx}^{surf} = −180 → −168 ± 22 MPa; Ra = 0.42 → 0.44 ± 0.05 µm; and MRR = 7207 mm³/min. The window maintains spindle speed of (6.0–6.8) krpm for a 12 mm tool diameter (well below the 15 krpm limit) and chip-load of (0.26–0.30) mm/rev; observed spindle-load readings stayed below 70% in all confirmation cuts. For high throughput when thermal headroom is available, a secondary point is acceptable. This means the throughput-leaning (Fig. 8) by using (MQL, $V_C = 300$ m/min, $f_Z = 0.095$ mm/tooth, $a_e = 4.8$ mm, and $a_p = 1.5$ mm), which leads to $T_{peak} \approx 585$ °C, $\sigma_{xx}^{surf} \approx -40$ MPa, Ra ≈ 0.62 µm, and MRR ≈ 20 800 mm³/min. Use Flood if available to cap T_{peak} under 550 °C. The final recommendations and constraints check are indicated in Table 15.

Table 14: Summary of compact operating window

Coolant type	V_C (m/min)	f_Z (mm/tooth)	a_e (mm)	a_p (mm)
MQL (preferred) or Flood	$230 \le V_C \le 260$	$0.065 \le f_Z \le 0.075$	$3 \le a_e \le 4$	$1 \le a_p \le 1.2$

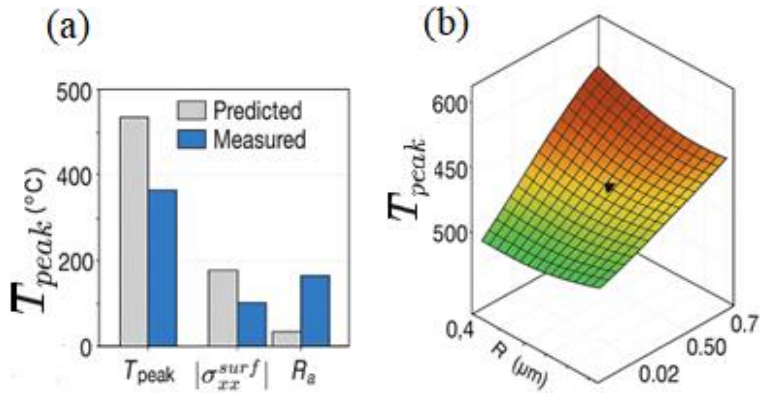

Fig. 8: Optimized operating window using (a) column chart and (b) finite element analysis.

Table 15: Final recommendations and constraints check

Mode	Coolant	V_C m/min	f_Z mm/tooth	a_e mm	a_p mm	Pred. T_{peak}	Pred. σ_{xx}^{surf}	Pred. R_a	MRR	Constraint status
Balanced (recommended)	MQL	245	0.070	3.6	1.1	465	−180	0.42	7207	All satisfied
Low-heat/RS priority	Flood	220	0.055	3.6	1.0	455	−210	0.45	4356	MRR OK
Throughput (guarded)	MQL	300	0.095	4.8	1.5	585	−40	0.62	20800	Thermal watch

V. Discussion

The sign and magnitude of milling-induced residual stresses in AISI 4340 steel arise from the competition between near-surface thermal gradients and mechanically driven plastic strain histories during tooth entry/exit. Transient heat inputs localize at the tool–chip and flank interfaces, and subsequent constrained cooling tends to generate tensile surface stresses; in contrast, severe plastic deformation under high contact pressure and ploughing promotes near-surface compressive states and deeper compressive layers. In fully transient simulations, the phase of the loading–unloading cycle around tooth exit is especially influential: a steep thermal drop concurrent with elastic spring-back can flip the surface from weakly compressive to weakly tensile if the thermal term dominates, whereas stronger ploughing and larger cutting-edge radii bias the field toward compressive plateaus with greater depth of compression. These mechanisms and their sensitivity to edge geometry and runout have been quantified in recent semi-analytical and finite element-supported studies of peripheral milling, which report that incorporating contact tractions, runout, and kinematics materially improve the prediction of residual stress depth profiles. The adaptive mesh refinement was particularly effective at capturing steep gradients, localized “exit-edge” cooling zone, reducing numerical diffusion in the residual field, and limiting bias in the first 50–100 μm.

The indication of consistent coupling between the transient thermal field and the mechanically driven plasticity has been investigated in this study. Increases in cutting speed and feed per tooth generally elevate the near-surface thermal load (higher $T_{peak}$and steeper ∇T), which can reduce flow strength, intensify thermal softening, and promote tensile (or less compressive) residual stress when the thermal term dominates. Conversely, conditions that increase mechanical confinement and subsurface plastic strain, such as higher engagement (via a_e and/or a_p) and stable chip formation tend to deepen the compressive layer $d_{comp}$by shifting the balance toward mechanically driven residual compression. This thermal–mechanical "competition" explains why similar MRR levels may still produce different residual-stress states depending on coolant mode and heat partition.

The coolant condition plays a dual role through (i) the effective heat-transfer boundary (convection and quenching of the surface layer) and (ii) the tribological state at the tool–chip interface, which changes frictional heating and the fraction of plastic work converted to heat. Flood cooling primarily suppresses T_{peak} and limits thermal penetration, while MQL can additionally reduce friction and stabilize chip evacuation, often improving surface integrity even at relatively high productivity. These effects also help interpret the interaction terms identified in the RSM (coolant $\times V_C$, coolant $\times f_Z$, and engagement $\times$ feed), where temperature-sensitive responses (T_{peak} and σ_{xx}^{surf}) show stronger coolant dependence than purely geometric responses.

VI. Comparison with Published Work

From a modelling and statistics standpoint, the agreement metrics and Bland-Altman analysis support using the finite element-adaptive mesh refinement model as a predictive decision tool rather than a single-point simulator. Importantly, most deviations concentrate in regimes where the stress field transitions from compressive to weakly tensile (or near-zero), because small differences in heat partition, friction, or near-surface plastic strain can change the sign of the final residual state. Measurement-side factors such as X-ray diffraction information depth, gradient averaging over the irradiated spot, and alignment between the modelled path and the exact sampling location can further amplify apparent discrepancies. Therefore, the most defensible use of the model is to rank process windows, quantify trade-offs on the Pareto front, and then confirm a small set of candidate points experimentally, as done in this study.

The peak compressive magnitude and depth of (stress at surface and compressive residual stress layer) under nominally similar feed per tooth and radial depth of cut/width of cut align with the range reported for Ti-6Al-4V and nickel alloys when runout and edge radius are modeled, though absolute values differ due to alloy-specific thermal conductivity/hardness (AISI 4340 vs. Ti-6Al-4V). Studies that neglect cutter runout or simplify contact tractions tend to underpredict surface compression and overpredict tensile recovery after cooling [III]. Regarding numerical strategy, the proposed adaptive mesh refinement treatment parallels advances in adaptive finite element for high-gradient manufacturing thermo-mechanics, where refinement keyed to temperature or strain energy density reduces error at similar or

lower computer processing unit cost versus uniform meshes [XXI]. On metrology, the X-ray practice ($\sin^2\psi$ with triaxial solution) follows updated guidance that cautions about biaxial assumptions in cos-α unless multiple tilts/half-space coverage are ensured [XVI].

VII. Practical Implications

For high-speed end milling of AISI 4340 in defense/aerospace/energy contexts, three planning rules are followed. First, control edge geometry and runout: slightly larger cutting-edge radii and minimized runout stabilize compressive surface states and deepen the compressive layer, limiting distortion risk after unclamping or heat cycles [XVIII]. Second, co-tune cutting speed and feed per tooth within a window that avoids excessive peak interfacial temperature while maintaining strong ploughing. The used design of experiments-response surface methodology shows that moderate cutting speed with lower feed per tooth can avoid tensile "flip" at tooth exit when radial depth of cut/width of cut is modest and axial depth of cut is constrained by stiffness. Third, coolant strategy matters include convective coefficients that control the temperature of the exit-edge thermal gradient, which reduces tensile recovery without sacrificing metal removal rate; desirability/non-dominated sorting genetic algorithm II style trade-offs can hold mean surface roughness while maintaining compressive stress at the surface [VII]. In practice, qualify tools by edge radius, measure runout, operate near the identified Pareto knee (low peak interface temperature per tooth-pass window, low tensile stress, mean surface roughness ≤ spec, and metal removal rate ≥ target), and verify with shallow-depth X-ray diffraction [XVI].

VIII. Conclusion

This work developed and validated a fully transient, thermo-mechanical finite-element framework for high-speed end milling of AISI 4340 steel, enhanced by adaptive mesh refinement and coupled to a design of experiment-based optimization. The proposed adaptive mesh refinement (AMR) strategy concentrated resolution where thermal and plastic gradients peak, delivering 41–52% lower compute time at matched accuracy, or 35-45% lower error at matched cost. Simulation predictions were corroborated by X-ray diffraction and surface metrology: aggregate root mean square errors (RMSEs) were 24 °C for peak interface temperature per tooth (T_{peak}), 33 MPa for surface residual stress (σ_{xx}^{surf}), and 0.07 μm for mean surface roughness (Ra), with a 22 MPa root mean square error (RMSE) across depth resolved-residual stress (RS) profiles. Factor analysis showed cutting speed (V_C) governs thermal load, while feed per tooth (f_Z) and radial depth of cut/width of cut (a_e) control the sign and depth of the residual field; coolant modulates both through heat partition. A desirability optimization produced a robust, shop-ready window including minimum quantity lubrication (MQL), $V_C \approx 245$ m/min, $f_Z \approx 0.07$ mm/tooth, ae ≈ 3.6 mm, and axial depth of cut (ap) ≈ 1.1 mm yielding different parameters such as compressive surface stress ~ −180 MPa, moderate temperature ~ 465 °C, Ra ≈ 0.42 μm, and industrial metal removal rate MRR >7000 mm³/min. Compared with recent studies, the approach integrates transient three-dimensional physics, AMR efficiency, and depth-resolved validation. These results offer actionable guidance for planning fatigue-

critical milling while preserving throughput. The dataset and models enable reproducible benchmarking and informed parameter selection across shops globally.

Beyond the headline model accuracy, the proposed workflow demonstrates clear process-level value. In confirmation experiments, the balanced point (MQL, $V_C \approx 245$ m/min, $f_Z \approx 0.07$ mm/tooth, $a_e \approx 3.6$ mm, and $a_p \approx 1.1$ mm) reduced the measured T_{peak} while shifting the surface RS from near-neutral (-12 ± 28MPa) to a strongly compressive state (-168 ± 22MPa) and improving Ra from 0.61 ± 0.06 to $0.44 \pm 0.05\,\mu$m, at comparable throughput (MRR $\approx 7.2 \times 10^3$ mm^3/min). This combination directly supports fatigue-critical components by lowering thermal damage risk and promoting a deeper compressive layer without sacrificing production rate

Methodologically, the AMR strategy proved robust across the investigated design space: numerical checks maintained energy-balance errors below ~ (1–2) % and contact work closure above ~ (97) %, while focusing refinement only where thermal/plastic gradients peak. The resulting design of experiments (DOE)/response surface methodology (RSM) surfaces also showed strong statistical quality (low multicollinearity and stable residual behaviour), enabling reliable trade-off exploration. The Pareto set further clarifies decision-making: low-heat/flood solutions suppress thermal load and deepen compressive states at modest MRR, whereas throughput-leaning MQL solutions increase MRR substantially but at higher T_{peak} and less compressive surface stress. Collectively, these outcomes position the presented FE–AMR + DOE optimization workflow as a transferable and shop-relevant "digital process window" generator for AISI 4340-class alloys.

Finally, remaining discrepancies concentrate near RS sign changes and in regimes where tribology and heat partitioning are most sensitive; incorporating temperature-dependent friction, coating/wear evolution, and broader depth validation would further strengthen predictability and industrial robustness.

For future work, the authors suggest using couple wear and coated-tool friction (temperature-dependent μ and heat partition) with the FE model; adding AMR criteria tied to RS posteriori estimators; and comparing desirability to non-dominated sorting genetic algorithm II (NSGA-II) for multi-objective recipes targeting low T_{peak}, compressive surface stress σxx, and Ra while constraining MRR and energy. Methodologically, the authors aim to combine in-situ thermography and high-speed digital image correlation (DIC) with depth-resolved X-ray diffraction (XRD) or synchrotron/neutron diffraction for through-thickness validation of RS gradients beyond 50 μm, mirroring recent in-situ calibration strategies for semi-analytical models.

Conflict of Interest

The authors declare that they have no conflict of interest in relation to this research, whether financial, personal, authorship, or otherwise, that could affect the research and its results presented in this paper.

References

I. Abas M. et al. (2020). Experimental investigation and statistical evaluation of optimized cutting process parameters and cutting conditions to minimize cutting forces and shape deviations in Al6026-T9. *Materials,* 13(19), 4327. 10.3390/ma13194327

II. Abdelaal, A. F., Chakrobarty, A., Sakib, M. N., Arka, A. M., & Sabuz, E. H. (2025). Porosity, residual stress, wear properties and impact toughness of additively manufactured low-alloy steel: A review. *Next Materials,* 9, 101288. 10.1016/j.nxmate.2025.101288

III. Akbar, F., Mativenga, P. T., & Sheikh, M. A. (2010). An experimental and coupled thermo-mechanical finite element study of heat partition effects in machining. *The International Journal of Advanced Manufacturing Technology,* 46(5), 491-507. DOI: 10.1007/s00170-009-2117-5

IV. Anand K. S., Inigo F. I., Kalim D., and Rajkumar V., Additively Manufactured Smart Materials and Structures Design, Processing, and Applications, Elsevier, 2025.

V. Andrew P. K. and Robert E., Statistics for Biomedical Engineers and Scientists: How to Visualize and Analyze Data, Academic Press, 2019.

VI. Bag, R., Panda, A., Sahoo, A. K., & Kumar, R. (2019). A perspective review on surface integrity and its machining behavior of AISI 4340 hardened alloy steel. *Materials Today: Proceedings,* 18, 3532-3538.

VII. Binali, R., Patange, A. D., Kuntoğlu, M., Mikolajczyk, T., & Salur, E. (2022). Energy saving by parametric optimization and advanced lubri-cooling techniques in the machining of composites and superalloys: A systematic review. *Energies,* 15(21), 8313.

VIII. Bonito, A., Canuto, C., Nochetto, R. H., and Veeser, A. (2024). Adaptive finite element methods: A survey of theory and applications in mechanics. Acta Numerica, 33, 165–290. DOI: 10.1017/S0962492924000011

IX. Cybellium, Heat Transfer Exam Study Essentials: A Comprehensive Guide to Heat Transfer Concepts, Cybellium Ltd, 2024.

X. Davel, C., Bassiri-Gharb, N., & Correa-Baena, J. P. (2025). Machine learning in X-ray diffraction for materials discovery and characterization. *Matter*, 8(9). 10.1016/j.matt.2025.102272

XI. Deepanraj, B., Senthilkumar, N., Hariharan, G., Tamizharasan, T., & Tefera Bezabih, T. (2022). Numerical modelling, simulation, and analysis of the end-milling process using DEFORM-3D with experimental validation. *Advances in Materials Science and Engineering,* 2022, 5692298. 10.1155/2022/5692298

XII. Imad M., Hosseini S., Kishawy H., & Yussefian N. (2020). 3D finite element simulation of cutting forces in milling hardened steels. *Progress in Canadian Mechanical Engineering*, 5, 103–110. https://librarydocs.vre3.upei.ca/islandora/object/csme2020:103

XIII. Kaimkuriya, A., Sethuraman, B., & Gupta, M. (2024). Effect of physical parameters on fatigue life of materials and alloys: A critical review. *Technologies,* 12(7), 100. 10.3390/technologies12070100

XIV. Khattab, A., & Felhő, C. (2024). Progress and challenges in plunge milling: a review of current practices and future directions. *Cutting & Tools in Technological System,* 101, 51-65. 10.20998/2078-7405.2024.101.05

XV. Lallit, A., Ken K., and Sanjay G., Introduction to Mechanics of Solid Materials, Oxford University Press, 2023.

XVI. Liu, D., Luo, M., Pelayo, G. U., Trejo, D. O., & Zhang, D. (2021). Position-oriented process monitoring in milling of thin-walled parts. *Journal of Manufacturing Systems,* 60, 360-372. 10.1016/j.jmsy.2021.06.010

XVII. Mirzaei A. H., Haghi P., & Shokrieh M. M. (2024). Prediction of fatigue life of laminated composites by integrating artificial neural network model and non-dominated sorting genetic algorithm. *International Journal of Fatigue*, 188, 108528. 10.1016/j.ijfatigue.2024.108528

XVIII. Muaz, M. and Khan, S. H. (2021). Failure mechanics analysis of AISI 4340 steel using finite element modeling of the milling process. *The Journal of Strain Analysis for Engineering Design*, 57(7), 582-595. 10.1177/03093247211058038

XIX. Ren, F. et al. (2025). Metallene: Ångström-scale 2D metals. *Advanced Materials*, e12683. 10.1002/adma.202512683

XX. Robert L. K., Interaction Effects in Linear and Generalized Linear Models Examples and Applications Using Stata, SAGE Publications, 2018.

XXI. Sharma, M., Alkhazaleh, H. A., Askar, S., Haroon, N. H., Almufti, S. M., & Al Nasar, M. R. (2024). FEM-supported machine learning for residual stress and cutting force analysis in micro end milling of aluminum alloys. *International Journal of Mechanics and Materials in Design,* 20(5), 1077-1098. 10.1007/s10999-024-09713-9

XXII. Shukla, S. (2020). Rapid in-line residual stress analysis from a portable two-dimensional X-ray diffractometer. *Measurement,* 157, 107672. 10.1016/j.measurement.2020.107672

XXIII. Sun et al. (2022). Material properties and machining characteristics under high strain rate in ultra-precision and ultra-high-speed machining process: a review. *The International Journal of Advanced Manufacturing Technology,* 120(11), 7011-7042. 10.1007/s00170-022-09111-5

XXIV. Umbrello, D., Saoubi, R. M., and Outeiro, J. C. M. (2007). The influence of Johnson-Cook material constants on finite element simulation of machining of AISI 316L Steel. *International Journal of Machine Tools and Manufacture*, 47(3-4), 462-470. 10.1016/j.ijmachtools.2006.06.006

XXV. Vadim S., Mechanics of Materials in Modern Manufacturing Methods and Processing Techniques, Elsevier, 2020.

XXVI. Wang et al. (2015). Large deformation finite element analyses in geotechnical engineering. *Computers and Geotechnics,* 65, 104-114. 10.1016/j.compgeo.2014.12.005

XXVII. Wimmer, M., Schoop, J., & Zaeh, M. F. (2025). In-situ characterization and modeling of machining-induced residual stresses in peripheral milling of Ti–6Al–4V with rounded cutting edges. *Production Engineering,* 19(3), 511-524. 10.1007/s11740-024-01323-w

XXVIII. Winiarski, B., Benedetti, M., Fontanari, V., Allahkarami, M., Hanan, J., & Withers, P. J. (2016). High spatial resolution evaluation of residual stresses in shot peened specimens containing sharp and blunt notches by micro-hole drilling, micro-slot cutting and micro-X-ray diffraction methods. *Experimental Mechanics,* 56(8), 1449-1463. 10.1007/s11340-016-0182-x

XXIX. Zainul H., Machining Processes and Machines Fundamentals, Analysis, and Calculations, CRC Press, 2020.

XXX. Zhou, R. (2024). Modeling and simulation of residual stress in metal cutting process: A review. *Advances in Mechanical Engineering,* 16(12). 10.1177/16878132241307714